ACS APPLIED MATERIALS & INTERFACES

www.acsami.org

Research Article

Photoswitchable CRISPR/Cas12a-Amplified and Co_3O_4@Au Nanoemitter Based Triple-Amplified Diagnostic Electrochemiluminescence Biosensor for Detection of miRNA-141

Qian Wang,[‖] Zuhao Zhang,[‖] Lu Zhang, Yunqing Liu, Li Xie,* Shenguang Ge,* and Jinghua Yu

Cite This: *ACS Appl. Mater. Interfaces* 2022, 14, 32960−32969

Read Online

ACCESS | Metrics & More | Article Recommendations | Supporting Information

ABSTRACT: In this work, a CRISPR/Cas12a initiated switchable ternary electrochemiluminescence (ECL) biosensor combined with a Co_3O_4@Au nanoemitter is presented for the in vitro monitoring of miRNA-141. Benefiting from the advantages of high-throughput cargo payload capability and superconductivity, three-dimensional reduced graphene oxide (3D-rGO) was designated as an introductory conducting stratum of a paper working electrode (PWE). With the collaborative participation of Co_3O_4@Au NPs, the transmutation of TPrA in the $Ru(bpy)_3^{2+}$/TPrA system can be riotously expedited into exorbitant free radical ions $TPrA^{\bullet}$, which provoked the exaggeration of the ECL signal. Moreover, the programmable enzyme-free hybrid chain reaction (HCR) amplifier on the PWE surface accurately anchored the assembly of nucleic acid tandem and accomplished the secondary recursion of the signal. Impressively, the multifunctional CRISPR/Cas12a with nonspecific cis/trans-splitting decomposition manipulated the photoswitch of the "on−off" signal state that avoided the false-positive diagnosis. The presented multistrategy cooperative biosensor demonstrated extraordinary sensitivity and specificity, with a low detection limit of 3.3 fM (S/N = 3) in the concentration scope from 10 fM to 100 nM, which fully corresponded to the expectation. Overall, this innovative methodology paved a generous avenue for evaluating multifarious biotransformations and provided a tremendous impetus to the development of real-time diagnosis and clinical detection of other biomarkers.

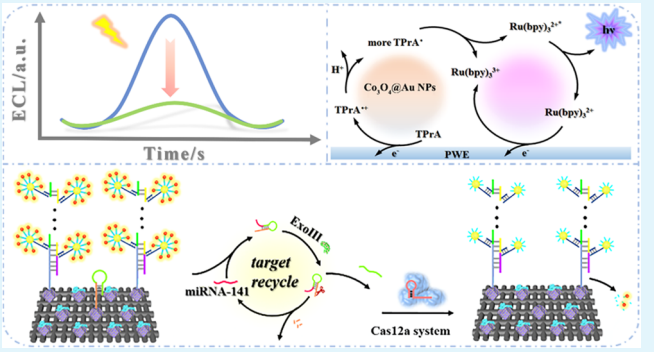

KEYWORDS: *electrochemiluminescence, CRISPR/Cas12a, hybridization chain reaction, microRNA-141, Co_3O_4@Au nanoparticles*

1. INTRODUCTION

Cancer, malignant tumors, autoimmune deficiency diseases, and degenerative neurological diseases are all threatening human life and health all the time, which raises numerous challenges to the diagnosis and treatment according to the World Health Organization (WHO).[1,2] MicroRNA (miRNA), as a short nucleic acid sequence, can control the malignant expression and biological activities of many gene, making it an innovative approach for the preliminary touch and discharge and prognosis recovery of these major diseases.[3−5] Therefore, the excavation of rapid, efficient, and ultrasensitive detection technology of miRNA can not only precipitate the detection rate of diseases effectively but also retrench the window period of pathogen detection greatly.[6,7] At present, the technologies that have been explored incorporate surface-enhanced Raman spectroscopy (SERS),[8] fluorescence (FL),[9] photoelectrochemistry (PEC),[10] chemiluminescence, and electrochemiluminescence (ECL)[11,12] and have shown preeminent practical implications. Among them, ECL has captivated increasingly deliberation and brilliance owing to the minimal background noise, ultrahigh sensitivity, extremely low detection limit, and admirable electrochemical performance and has become an indispensable part in the areas of clinical medicine, food security, environmental monitoring, and so on. In the past few decades, ECL luminophores have been cultivated from luminol, $Ru(bpy)_3^{2+}$, and other classical reagents to quantum dots and metal nanoclusters.[13] To substantially exaggerate the transmission electronically intensity of luminophores, penalize the disadvantages of ambiguous registration, and escape the quite hazards of co-reaction reagents,[14] the competitive co-reaction projectors (including aniline substances,[15] metal complexes,[16] noble metal nanoparticles, and semiconductor nanomaterials[17,18]) are familiarized with the conventional binary ECL system, which can trigger a qualitative leap in signal enhancement.

Received: May 18, 2022
Accepted: July 6, 2022
Published: July 15, 2022

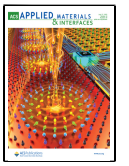

Scheme 1. (A) Synthesis Scheme of Co_3O_4@Au NPs. (B) Stripping Preparation of 3D-rGO. (C) Schematic Illustration of the CRISPR/Cas12a-Based ECL Biosensor

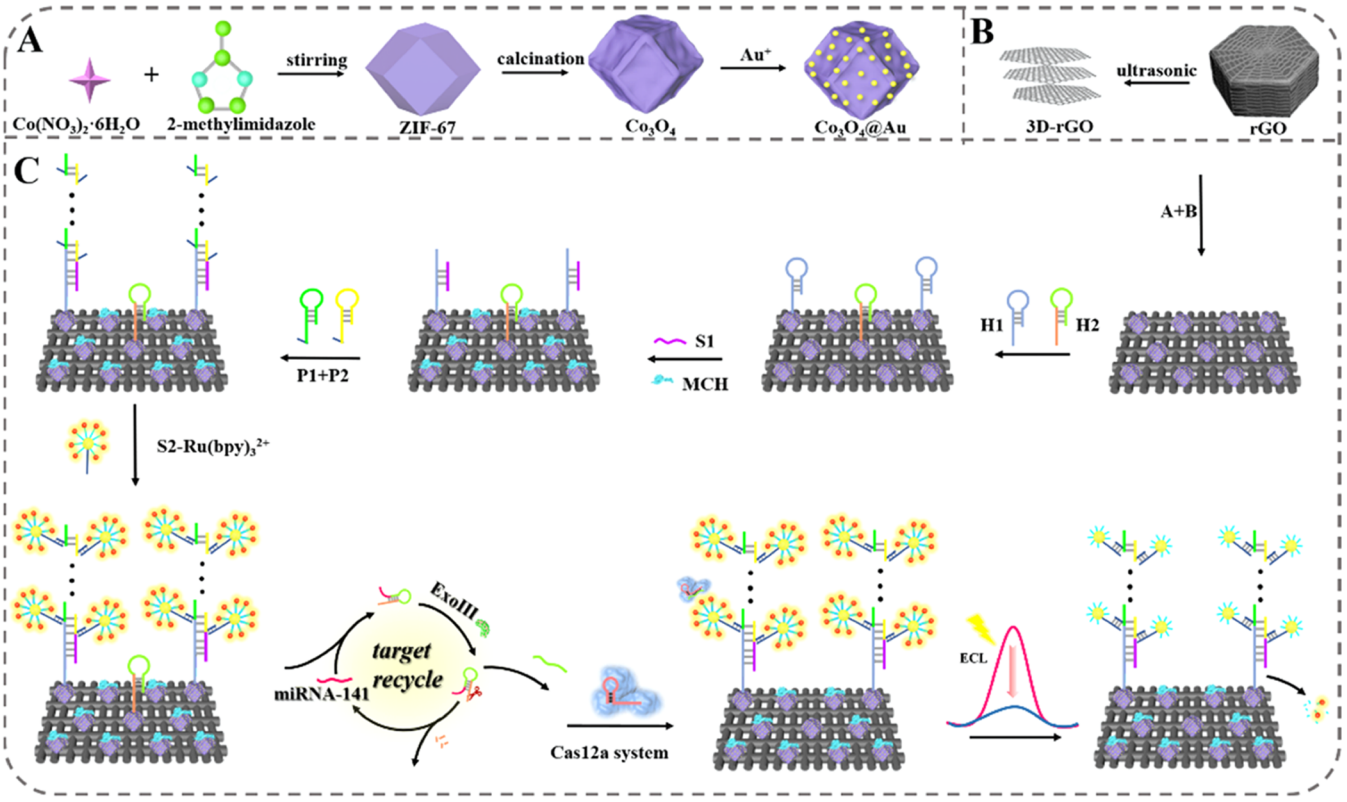

In addition to chemical enhancement factors that can manipulate the sensitivity of redox reaction, visualize powerful genetic tools and molecular machines at the biological level can also exponentially duplicate the concentration of targets at in trace standard. Nucleic acid amplification technologies including DNA walker,[19,20] catalytic hairpin self-assembly (CHA),[21] rolling circle amplification (RCA),[22] and hybridization chain reaction (HCR)[23] play a fundamental role in bioanalysis. In particular, the isothermal amplification HCR technology, which is on account of the chain reaction of recognition and hybridization between a couple of complementary and dynamically captured hairpins, provides an incomparable amplification opportunity for short-sequence oligonucleotides.[24,25] For example, based on in situ synthesized silver nanoclusters (Ag NCs) as a signal probe, a triple amplification biosensor for ultrasensitive methyltransferase (Dam-MTase) activity detection and inhibitor screening was constructed using gold nanoparticles/electrochemically reduced graphene oxide (Au nanoparticles (NPs)/ERGO) composite and HCR amplification current signal-coupling effect, which was reported by Peng et al.[26]

Indeed, under the premise of adequate signal amplification, ultrasensitive and fast-forward conversion of the signal is still required. As an adaptive immune system for invading nucleic acid phages in archaea, the clustered regularly interspaced short palindromic repeat (CRISPR)/Cas system has been extensively applied to the fields of gene editing and biomedical engineering since it was first disinterred in *Escherichia coli*.[27,28] In fact, it not only punctures the barrier of sodium bisulfite genomic sequencing but also dominates the biological activities of nuclease precisely, bursting out a forceful influence of species iteration. The relatively mature Cas proteins such as Cas9,[29] DETECTR of Cas12a,[30] HOLMES,[31] and SHERLOCK[32] of Cas13a endow CRISPR/Cas with a particular mission of their unique double-cutting performance and hew out a prospective path for rapid molecular diagnosis. Especially in the competition of micro-biomarker investigation, Cas12a technique possesses higher sensitivity, lower material consumption, and commendable accurate specificity,[33−35] profiting from the precise attribute manipulation of DNase and the perspicacious excision of oligonucleotide, effecors can apprehend reporters instantaneously and further trigger nonspecific trans-splitting occupation. As the most qualified low-energy consumption burgeoning technique, lab-on-paper device (LPD) has raised the wave of efficient minimalism in the construction of biosensors owing to the extremely low-cost, microflow channel programmability, no external pumping system, 3D permeability characteristics, and immediate visual diagnosis.

In this study, based on the photoswitchable trans-splitting of CRISPR/Cas12a, a ternary ECL paper-based biosensor guided by HCR for ultrasensitive detection of miRNA-141 to realize real-time diagnosis of diseases was presented. As shown in Scheme 1A, the Co_3O_4@Au NP composite[36] was synthesized by a hydrothermal method, while three-dimensional reduced graphene oxide (3D-rGO) was delaminated from chunky by ultrasonic crushing (Scheme 1B). And then, they were embellished on the paper working electrode (PWE)[37−40] to formulate an exceptional conductive layer and a co-reaction catalytic layer. As shown in Scheme 1C, H1 + H2 hairpins were grafted onto the Au NPs surface via the sulfhydryl group (−SH)[41] and incubated on the PWE. After the introduction of the S1 primer, the hairpin structure of H1 could be automatically opened and paired with a double-chain base.

https://doi.org/10.1021/acsami.2c08823
ACS Appl. Mater. Interfaces 2022, 14, 32960−32969

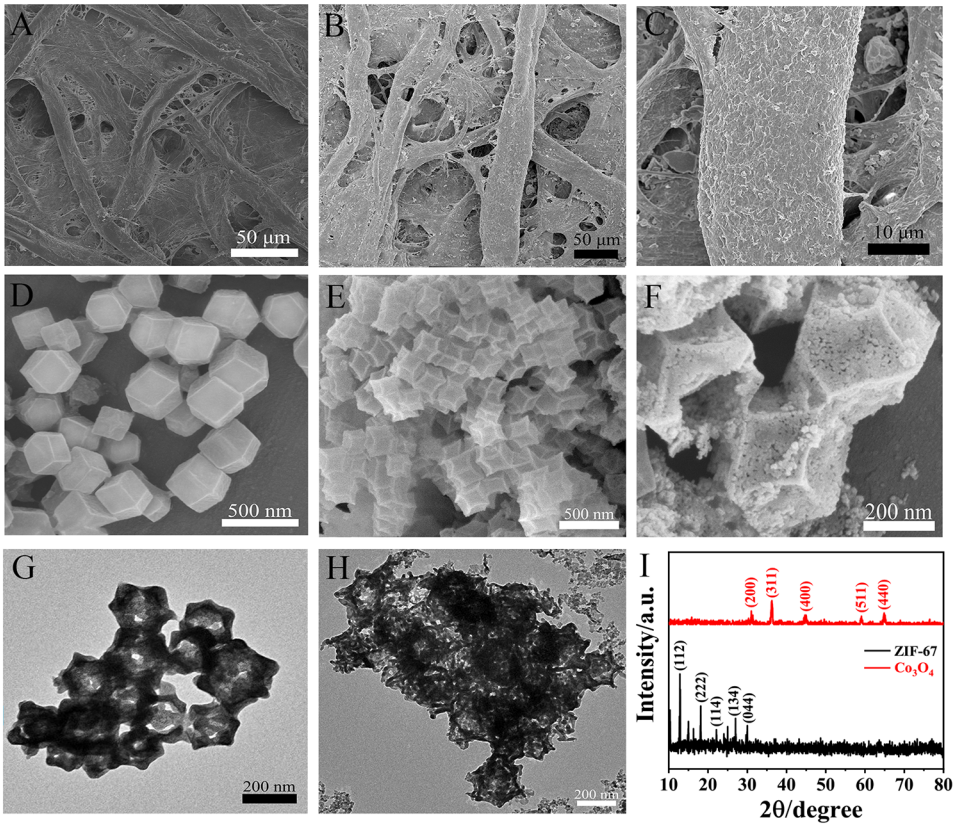

Figure 1. SEM images of (A) bare paper, (B) 3D-rGO/PWE, (C) magnified 3D-rGO/PWE, (D) ZIF-67, (E) Co_3O_4 polyhedron, and (F) Co_3O_4@Au NPs. TEM images of (G) Co_3O_4 and (H) Co_3O_4@Au NPs. (I) XRD analysis of ZIF-67 and Co_3O_4.

At this time, the arrival of 6-mercapto-1-hexanol (MCH) would shelter the remaining active sites at the PWE interface and prevent the grafting from subsequent nucleotide chains. After P1 + P2 hairpins were introduced, the HCR reaction process could be touched off and long DNA double-stranded structures could be constituted through the principle of specific recognition sites and Watson−Crick base complementary pairing. Subsequently, the $Ru(bpy)_3^{2+}$ labeled spherical nucleic acid (SNA)[42] was incubated to the electrode surface and reached the "signal on" state through the combination of the support probe and the bifurcation part of the long DNA strands. The specific cleavage of DNase and the circulation of the target were implemented by the arrival of miRNA-141 and exonuclease III (ExoIII). However, with the involvement of Cas12a protein, the loop region of H2 could be captured by CRISPR/Cas12a + crRNA to forge a diploid, which completely activated the trans-flanking cleavage performance and nonspecifically digested all single-stranded DNAs on the surface of PWE. After a period of cutting, S2-$Ru(bpy)_3^{2+}$ were completely cut off and the state converted to "signal off".

2. EXPERIMENTAL SECTION

2.1. Reagents and Instruments. The reagents and instruments are described in the Supporting Information.

2.2. Synthesis of Co_3O_4@Au NPs. In the light of the reported work, the Co_3O_4 polyhedron derived from ZIF-67 was synthesized with minor modifications.[43] In detail, 0.2910 g of $Co(NO_3)_2{\cdot}6H_2O$ was dissolved in 20 mL of methanol, while 0.6568 g of 2-methylimidazole was dissolved in 20 mL of methanol. After sufficient stirring, the latter was mixed into the former. The precipitate of the product ZIF-67 octahedron, which was statically aged at room temperature for 24 h, was washed three times with methanol and dried in a vacuum at 60 °C for 12 h. Then, the obtained intermediate product purple powder was calcined in a tubular furnace under an argon atmosphere at 350 °C for 30 min to maintain the morphology of the ZIF-67 regular octahedron, followed by oxidative calcination at this temperature for 30 min in the air (the color changes from bright purple to gray-black). Finally, the Co_3O_4 polyhedron transformed from the ZIF-67 octahedron could be successfully prepared. Immediately, 50 mg of Co_3O_4 polyhedron and 20 mL of $HAuCl_4$ (1 mM) were mixed into a 50 mL round-bottom flask and stirred constantly. While the above mixture was continuously heated to boiling, 5 mL of $Na_3C_6H_5O_7$ (38.8 mM) was rapidly introduced and the mixture was stirred vigorously for 15 min. Ultimately, the Co_3O_4@Au NP aqueous suspension (1 mg·mL^{-1}) was obtained after washing with ultrapure water four to five times.

2.3. Fabrication of the $Ru(bpy)_3^{2+}$-Labeled SNA. The fabrication of the $Ru(bpy)_3^{2+}$-labeled SNA was as follows. First, Au NPs were prepared on the basis of the traditional Turkevich method[44] (see the Supporting Information). Then, the $Ru(bpy)_3^{2+}$-labeled S2 (the report probe) (200 μL, 1 μM) and support probe (100 μL, 1 μM) were added to 500 μL of the Au NP solution and placed on a shaker for multibranched DNA assembly reaction at 25 °C for 12 h. Finally, the culture medium was centrifuged at 10000 rpm for 5 min and washed three times with enzyme-free water and the obtained $Ru(bpy)_3^{2+}$-labeled SNA was resuspended in 10 M Tris−HCl (pH = 7.4) for further use.

2.4. Construction of the CRISPR/Cas12a-Derived ECL Sensing Interface. According to relevant reports, prior to the procedure, all PWEs were treated by wax and screen printing technology (see the Supporting Information). DNA strands including H1, H2, P1, and P2 were annealed at 95 °C for 5 min and then gradually cooled to room temperature for more than 2 h to form a stable hairpin structure.

Specifically, 20 μL of 3D-rGO (2 mM) was modified on the PWE surface using a spin coater to form a conductive substrate and was

https://doi.org/10.1021/acsami.2c08823
ACS Appl. Mater. Interfaces 2022, 14, 32960−32969

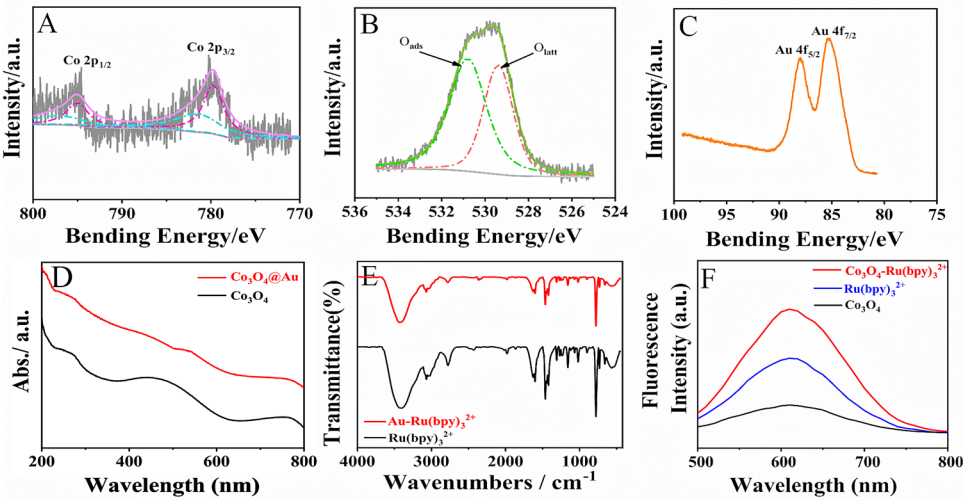

Figure 2. XPS analysis of (A) Co 2p, (B) O 1s, and (C) Au 4f. (D) UV−vis absorption spectrum of Co_3O_4 and Co_3O_4@Au NPs. (E) FTIR spectrum of $Ru(bpy)_3^{2+}$ and Au@ $Ru(bpy)_3^{2+}$. (F) fluorescence analysis of Co_3O_4@Au NPs, $Ru(bpy)_3^{2+}$, and Co_3O_4@Au NPs-$Ru(bpy)_3^{2+}$.

repeatedly dried and spin-coated at room temperature several times to obtain a gray-black hydrophilic region. After diluting the solution three times, the prepared 20 μL of Co_3O_4@Au NPs (1 mg·mL^{-1}) was modified on the PWE to construct an excellent conductive catalytic substrate. Next, 20 μL of the mixture of H1 and H2 hairpin (10^{-6} M) was incubated at 25 °C for 2 h and firmly bonded to PWE through the combination of the Au−S bond. After further incubating with 20 μL of a S1 primer probe (10^{-6} M) for 2 h, it could be specifically recognized and captured by H1 for complete matching of base pairs so as to open the H1 hairpin structure. Then, the remaining active sites on the PWE were blocked by 20 μL of MCH (1 mM) for 1 h and rinsed with phosphate buffer solution (PBS, 10 mM, pH = 7.4). Next, 20 μL of P1 and P2 hairpins (10^{-6} M) was introduced, which could be immediately distinguished by incomplete paired double-stranded DNA and grafted onto the PWE surface. After 3 h of constant-temperature incubation at 25 °C, the HCR amplification process was activated to form a large number of long double-stranded DNA structures. Immediately, the PWE interface with signal maximization was achieved by incubation at 25 °C for 4 h of 20 μL $Ru(bpy)_3^{2+}$-labeled SNA (10^{-6} M). Ultimately, after 20 μL of the mixture ExoIII and different concentrations of target miRNA-141 were incubated for 2 h, CRISPR/Cas12a (100 nM) and the incidental crRNA (120 nM) were incubated instantly for 1 h, which could enable H2 hairpin to be digested and motivated the flanking cleavage behavior of the CRISPR/Cas protein.

2.5. ECL Measurement Procedure. The ECL measurement was implemented in 100 μL of working solution, which contained 0.1 M TPrA and 10 mM PBS, and the scan potential range was 0−1.25 V and the scan rate was 100 mV/s. During the measurement operation, the voltage of the photomultiplier tube (PMT) was set at 800 V.

3. RESULTS AND DISCUSSION

3.1. Characterizations of the Prepared Nanomaterials. As shown in Figure 1A, the bare PWE substrate was distributed with crisscross fiber strips, and the scanning electron microscopy field of view was still dark after gold spraying due to the poor conductivity. As shown in Figure 1B, the 3D-rGO layer was densely and evenly coated on the fiber surface of the PWE substrate, which greatly improved the electron transmission rate and specific surface area. Through the magnified Figure 1C, each fiber was observed to be wrapped with folded 3D-rGO, which proved that the preparation and modification were successful. Moreover, the morphology, dimension, and crystal form of ZIF-67, Co_3O_4 polyhedron, and Co_3O_4@Au NP complex were revealed by SEM, transmission electron microscopy (TEM), and X-ray diffraction (XRD). As exhibited in Figure 1D, the ZIF-67 polyhedron calcined in the argon atmosphere of the tubular furnace was a regular dodecahedron structure, with an average size of about 300 nm. The MOF intermediate calcined in the oxygen atmosphere had an irregular dodecahedral structure with a rough and wrinkled surface, which produced dense active sites, stimulated the catalytic performance of Co_3O_4 as a co-reaction promoter, and reduced the particle size (Figure 1E). When Au NPs were fixed on the surface of Co_3O_4 by the original growth method, it could be observed that the outer layer of Co_3O_4 was coated with dense particles, which proved superior conductivity with a bright visual field (Figure 1F). Compared with the TEM image of the single Co_3O_4, the wrapped Co_3O_4 structure was more sparse and loose in the presence of Au NPs (Figure 1G,H). More evidence could be attributed to the characterization of XDR diffraction patterns. Several characteristic peaks of ZIF-67 were accurately consistent with previous reports. After further calcination, the characteristic peaks completely disappeared. Then, new characteristic peaks appeared at 31.3, 36.9, 44.8, 59.3, and 65.5°, which coincided with card JCPDS No. 42-1467 (Figure 1I).

In addition, the chemical composition and electronic valence state of Co_3O_4@Au NPs was determined by X-ray photoelectron spectroscopy (XPS) scanning. As shown in Figure 2A, in the high-resolution spectrum of Co 2p, two distinct characteristic peaks of Co $2p_{1/2}$ appeared at 796 eV, which belonged to Co $2p_{1/2}$ Co^{3+} (795.58 eV) and Co^{2+} (797.33 eV), respectively. Equivalently, two apparent characteristic peaks of Co $2p_{3/2}$ also emerged at 781 eV, which belonged to Co $2p_{3/2}$ Co^{3+} (780.52 eV) and CO^{2+} (782.67 eV), respectively. The characteristic of the high-resolution O 1s spectrum is shown in Figure 2B. The two fitting peaks with binding energies of about 530.8 and 529.6 eV were attributed to surface-adsorbed oxygen (O_{ads}) and lattice oxygen species (O_{lat}) in Co_3O_4, respectively. As for high-resolution Au 4f, an obvious characteristic peak appeared at 87.7 eV of Au $4f_{5/2}$, and the value was in accordance with the previous report that proved the reliable content of Au (Figure 2C). The UV−vis absorption spectrum of Co_3O_4@Au NPs showed an obvious red-shift of Au absorption peak at 520 nm (Figure 2D). According to Fourier

https://doi.org/10.1021/acsami.2c08823
ACS Appl. Mater. Interfaces 2022, 14, 32960−32969

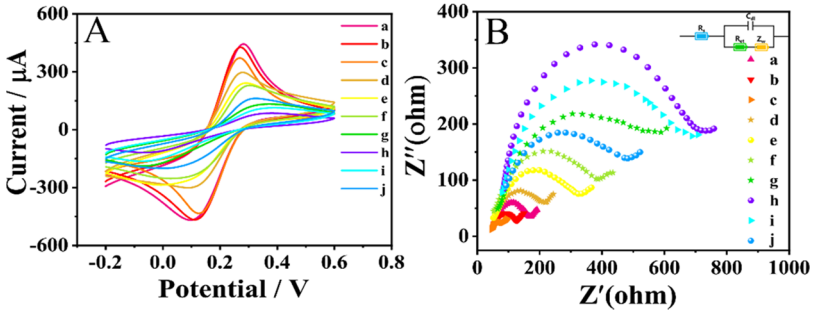

Figure 3. CV curve (A) and EIS spectrum (B) of the biosensor modification (in 5.0 mM $[Fe(CN)_6]^{3-/4-}$ including 0.1 M KCl): (a) bare PWE, (b) 3D-rGO/PWE, (c) Co_3O_4@Au NPs/3D-rGO/PWE, (d) H1 + H2/Co_3O_4@Au NPs/3D-rGO/PWE, (e) S1/H1 + H2/Co_3O_4@Au NPs/3D-rGO/PWE, (f) MCH/S1/H1 + H2/Co_3O_4@Au NPs/3D-rGO/PWE, (g) P1 + P2/MCH/S1/H1 + H2/Co_3O_4@Au NPs/3D-rGO/PWE, (h) S2-$Ru(bpy)_3^{2+}$/P1 + P2/MCH/S1/H1 + H2/Co_3O_4@Au NPs/3D-rGO/PWE, (i) miRNA-141 + ExoIII/S2-$Ru(bpy)_3^{2+}$/P1 + P2/MCH/S1/H1 + H2/Co_3O_4@Au NPs/3D-rGO/PWE, and (j) CRISPR/Cas12a + crRNA/miRNA-141 + ExoIII/S2-$Ru(bpy)_3^{2+}$/P1 + P2/MCH/S1/H1 + H2/Co_3O_4@Au NPs/3D-rGO/PWE.

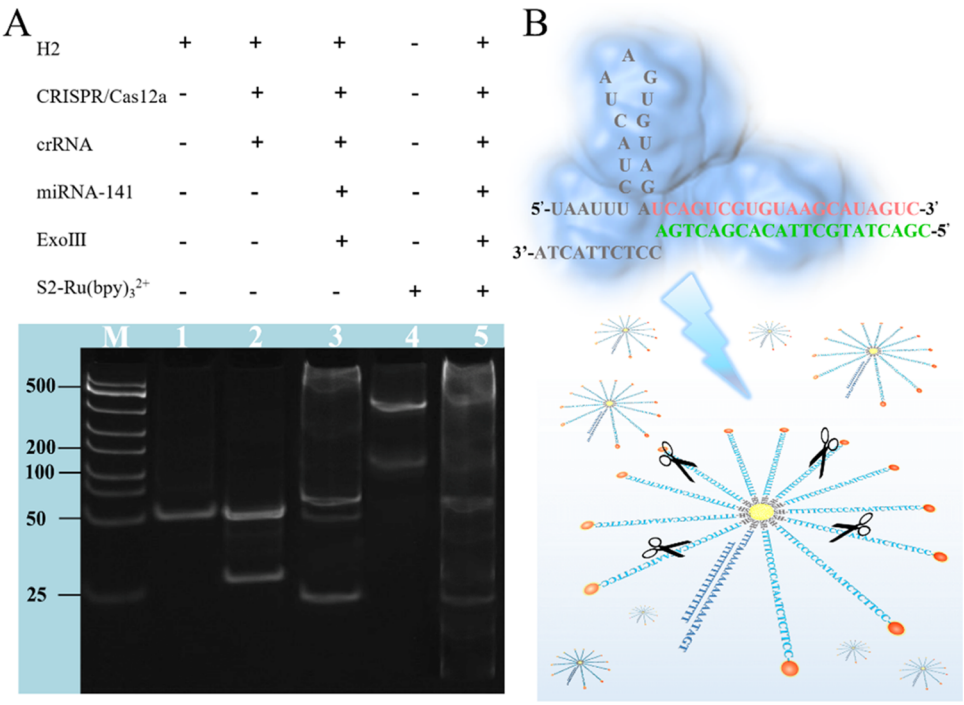

Figure 4. (A) PAGE image of flanking cleavage performance of CRISPR/Cas12a. M: DNA marker; lane 1: H2; lane 2: H2 + miRNA-141 + ExoIII; lane 3: H2 + miRNA-141 + ExoIII + CRISPR/Cas12a + crRNA; lane 4: S2-$Ru(bpy)_3^{2+}$; lane 5: H2 + miRNA-141 + ExoIII + CRISPR/Cas12a + crRNA + S2-$Ru(bpy)_3^{2+}$. (B) CRISPR/Cas12a trans-splitting schematic of base coding.

transform infrared (FTIR) analysis (Figure 2E), in the presence of $Ru(bpy)_3^{2+}$ alone, the characteristic peak exposed at 1627−1458 and 1437−1373 cm^{-1} might be owing to the skeletal vibration of bipyridine/benzene and the symmetric and asymmetric vibration of carboxylate anions, respectively. Two new fluctuates centered at 1600 and 1328 cm^{-1} in Au-$Ru(bpy)_3^{2+}$, which were distributed to the tensile vibration of C−O metal complexes, verifying the presence of the Au−O compounds. Moreover, the catalytic performance of Co_3O_4@Au NPs to $Ru(bpy)_3^{2+}$ fluorescence (FL) was studied under a 488 nm laser (Figure 2F). Although the FL intensity of $Ru(bpy)_3^{2+}$ was general, the FL effect of $Ru(bpy)_3^{2+}$ could be tremendously promoted when the nonfluorescence Co_3O_4@Au NPs were involved, which also proved that the catalytic effect of Co_3O_4@Au NPs as a co-reaction promoter was conspicuous.

3.2. Electrochemical Characterization of the Biosensor. To prove that biosensor was reasonable and feasible, CV scanning and electrochemical impedance spectroscopy (EIS) spectrum were implemented. As shown in Figure 3A (curve a), the fluctuation with a large distance between two peaks appeared on the surface of the bare PWE, indicating that the conductivity of the paper was poor. The current curve of the electrode interface modified by 3D-rGO expressed an upward trend, which was attributed to its excellent conductivity (curve b). When Co_3O_4@Au NPs were arranged in the 3D-rGO wrinkles intimately, the redox peak discrepancy reached the minimum, indicating that the modification of the PWE reached the maximum (curve c). Due to the nonelectrical conductivity of biological macromolecules, the peak separation was enlarged after the binding of H1 + H2 hairpins to the PWE surface through the Au−S bond (curve d). The sequential incubation of S1, MCH, and P1 + P2 not only

https://doi.org/10.1021/acsami.2c08823
ACS Appl. Mater. Interfaces 2022, 14, 32960−32969

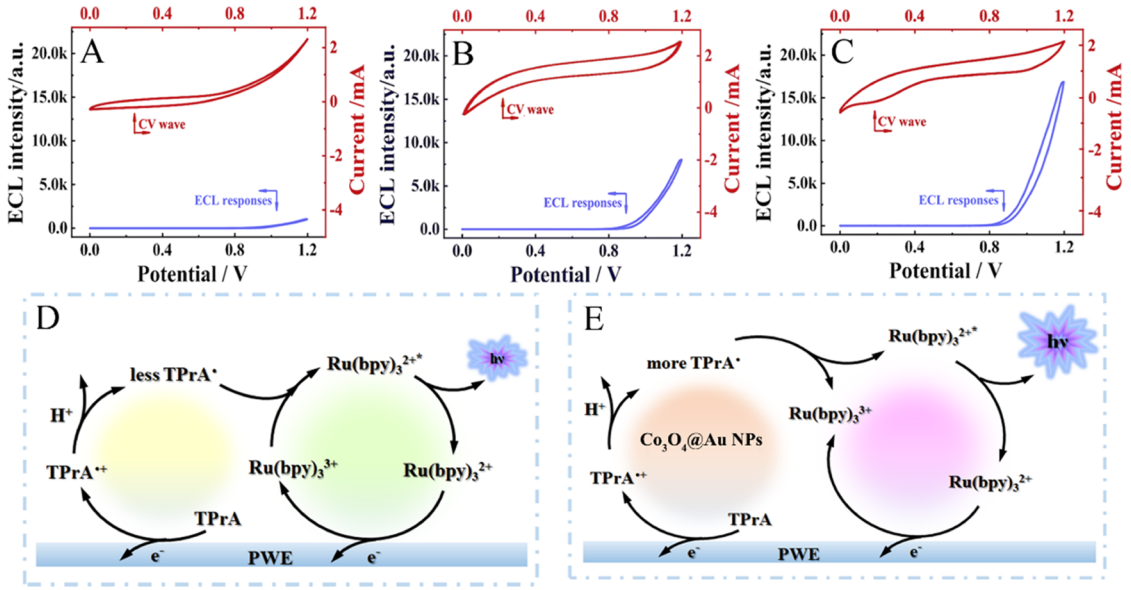

Figure 5. ECL potential distribution diagram (red line) and peak current of CV curve (green line) of (A) Co_3O_4@Au NPs, (B) Au NPs-$Ru(bpy)_3^{2+}$, and (C) Co_3O_4@Au NPs-$Ru(bpy)_3^{2+}$. (D, E) Schematic illustration of the ECL mechanism with or without Co_3O_4@Au NP.

activated the HCR reaction process and formed sufficient double-chain structures on the PWE surface rapidly but also increased the peak spacing (curve e–g). When $Ru(bpy)_3^{2+}$-labeled SNA was paired with the specific recognition of the 5′-end of P1 + P2, the ECL intensity of the PWE interface reached the peak and the conductivity reached a valley (curve h). Right after, when the target miRNA-141 and ExoIII were incubated on the electrode, they paired with H2 accurately and digested the 3′-end of the stem region, realizing the target circulation and reducing the PWE capacity (curve i). Eventually, the advent of CRISPR/Cas12a and crRNA could capture the circular region of H2 automatically to trigger the cleavage performance of Cas12a protein, which not only digested the single strand of all SNA nonspecifically but also led to explosive growth in conductivity (curve j).

As another method to characterize the feasibility of layer-by-layer modification steps, EIS was scanned in the frequency range of 0.1 Hz to 10 kHz. In the typical impedance spectrum, the efficiency and ability of the redox reaction process of the system were represented by the return electron transfer (RET) rate. As shown in Figure 3B, the bare paper displayed a large RET value (curve a), which may be due to the high resistance. To reduce the resistance of electron transfer, after modifying 3D-rGO and Co_3O_4@Au NPs, the RET value on the PWE surface reached a valley (curves b and c). However, with the introduction of H1 + H2, the RET value surged significantly (curve d). After the incubation of biomolecule S1 and blocking reagent MCH, the RET value increased further due to the enlargement of the steric hindrance (curves e and f). The incubation of P1 + P2 and the grafting of the $Ru(bpy)_3^{2+}$-labeled SNA resulted in the peak steric hindrance of the electrode and the maximum RET (curves g and h). Subsequently, the thorough incubation of target miRNA-141 and ExoIII could replace and digest the H2 on the electrode, and the RET produced a slightly declining trend (curve i). Finally, the participation of CRISPR/Cas12a + crRNA captured the replaced ring region of H2, which did not specifically cut all single strand structures on the electrode surface. The participation of CRISPR/Cas12a + crRNA captured the replaced ring region of H2, triggered the nonspecific cleavage property, and removed all luminescent substances were removed from the electrode interface, which caused a remarkable downward fluctuation of RET (curve j). The EIS spectrum was consistent with the conclusion of CV scanning, which demonstrated the successful construction of a biosensor.

To verify the feasibility of CRISPR/Cas12a-mediated flank cutting, a 12% polyacrylamide gel electrophoresis (PAGE) was used to detect the digestive effect of the support probe in an S2-labled SNA. The experimental results in Figure 4A certificated that there was no difference between the H2 probe (lane 1) and the H2 probe incubated with Cas12a + crRNA (lane 2), except for a new bright band of crRNA with low base content. After miRNA-141 and ExoIII were further involved, the dimeric structure captured by Cas12a appeared and the hairpin H2 structure was gradually digested (lane 3). Due to the strong steric hindrance effect, the migration rate of SNA loaded with high-molecular-weight nucleotides was slow in the electrophoresis process, leading to a higher bright band in lane 4. Surprisingly, with the disappearance of the characteristic bands of SNA in lane 5, a large number of fragmented DNA nanodevices appeared, indicating that the flanking cutting performance of CRISPR/Cas12a was thoroughly triggered for nonspecific digestion of the reported probes in SNA. The coding model of the base sequence was demonstrated in Figure 4B.

3.3. Characterization of the Effect of Co-Reaction Promoter on Signal Intensity. Since the luminescent $Ru(bpy)_3^{2+}$ expressed anode ECL activity with secure and steady, the effect of Co_3O_4@Au NPs on the luminescence intensity of $Ru(bpy)_3^{2+}$ was investigated. As shown in Figure 5A, when Co_3O_4@Au NPs were scanned to the positive potential individually, the changes in the ECL signal and cyclic voltammetry (CV) curve were faint, which verified its nonluminescence features. The ECL peak at 7500 au could be attributed to the autoluminescence signal caused by the redox reaction between $Ru(bpy)_3^{2+}$ and the co-reactant TPrA to produce a large amount of $TPrA^{\bullet+}$ (Figure 5B). However,

https://doi.org/10.1021/acsami.2c08823
ACS Appl. Mater. Interfaces 2022, 14, 32960–32969

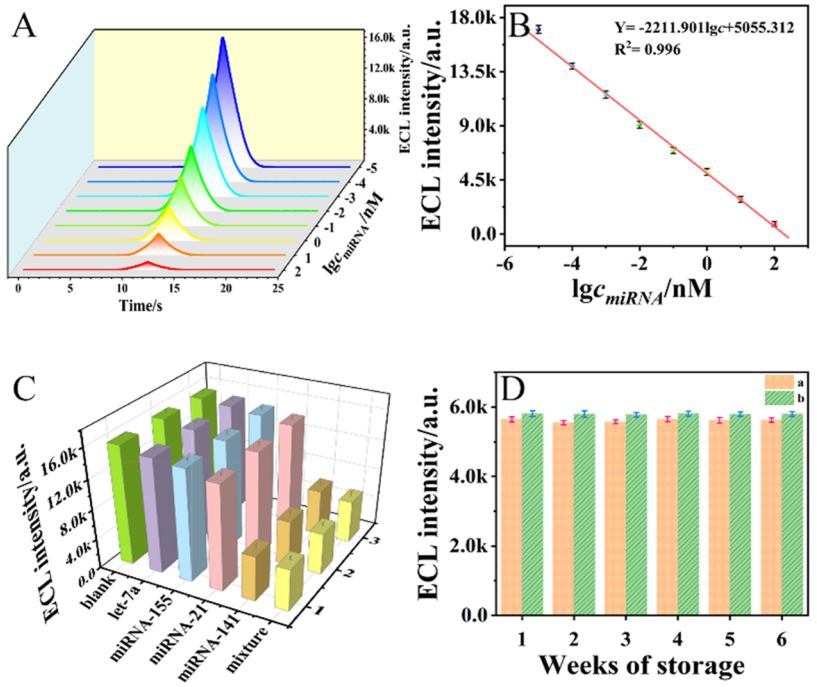

Figure 6. (A) ECL intensity−potential curves of the prepared biosensor incubated with miRNA-141 concentrations of 10 fM, 100 fM, 1 pM, 10 pM, 100 pM, 1 nM, 10 nM, and 100 nM. (B) Corresponding calibration for the relationship between the logarithm of miRNA-141 concentration and ECL intensity. (C) Selectivity of the biosensor with various interfering substrates: blank, 100 nM let-7a, 100 nM miRNA-155, 100 nM miRNA-21, 1 nM miRNA-141, and the mixture. (D) Stability of the biosensor (1 nM miRNA-141) at (a) room temperature and (b) in the refrigerator.

when the co-reaction promoter Co_3O_4@Au NPs participated in the system, the co-reactant was quickly catalyzed to produce more intermediate free radicals, which produced more excited state luminescence and exponentially enhanced the signal. At the same time, the peak current of the reduction peak increased, the voltage shifted in the negative direction (about 0.21 V), and the peak area expanded, which also successfully proved that Co_3O_4 can participate in the system and accelerate the reduction of $TPrA^{\bullet+}$ to more $TPrA^{\bullet}$ (Figure 5C).

3.4. Possible Mechanism of the Proposed ECL Biosensor. Owing to the powerful catalytic function and preeminent stability, Co_3O_4@Au NPs were selected as co-reaction promoters of $Ru(bpy)_3^{2+}$ anode ECL emission, and the possible reaction mechanism of the system was deduced. As shown in Figure 5D,E, with the excellent electronic transmission characteristics, Co_3O_4@Au NPs mediated excessive electron injection, which promoted the half-lived TPrA free radical cationic ($TPrA^{\bullet+}$) was forced to lose more protons from an α-carbon to produce vigorously reducing intermediate $TPrA^{\bullet}$. The emergence of a great quantity of such free radicals could transfer electrons to the π^* orbital of $Ru(bpy)_3^{2+}$ ligand and promote the reduction of $Ru(bpy)_3^{3+}$ to $Ru(bpy)_3^{2+*}$. As $Ru(bpy)_3^{2+*}$ decayed into the ground state, the energy was released in the form of an optical signal. The concrete enhanced principle was described by equations as follows

$$TPrA - e^- \xrightarrow{Co_3O_4@Au\ NPs} TPrA^{\bullet+} \quad (1)$$

$$TPrA^{\bullet+} - H^+ \rightarrow TPrA^{\bullet} \quad (2)$$

$$Ru(bpy)_3^{2+} - e^- \rightarrow Ru(bpy)_3^{3+} \quad (3)$$

$$TPrA^{\bullet} + Ru(bpy)_3^{3+} \rightarrow Ru(bpy)_3^{2+*} \quad (4)$$

$$Ru(bpy)_3^{2+*} \rightarrow Ru(bpy)_3^{2+} + h\nu \quad (5)$$

3.5. Analytical Performance of the ECL Biosensor. To evaluate the sensitivity of the biosensor, different concentrations of target miRNA-141 were detected. As shown in Figure 6A, in the concentration range of 10 fM to 100 nM, the ECL signal intensity gradually decreased with the increment of miRNA-141 concentration, indicating that more vitality CRISPR/Cas12a flanking cleavage effect led to more illuminants being stripped from the electrode surface. Under the optimal conditions (see the Supporting Information), there was a desirable linear relationship between the ECL intensity and the logarithm of miRNA-141 concentration (Figure 6B). The standard curve of the corresponding functional relationship fitting regression equation could be expressed as $I = -2211.90 \lg c_{miRNA} + 5055.31$ ($R^2 = 0.996$), and the minimum detection limit was 3.3 fM. The experimental results testified that the designed biosensor equipped with a wide working range and a low detection limit could realize the efficient and ultrasensitive detection of miRNA-141.

The accuracy of biosensor detection was largely influenced by anti-interference. Therefore, under optimal conditions, let-7a, miRNA-155, and miRNA-21 were selected as possible interference factors to replace miRNA-141 to evaluate the selectivity of the proposed biosensor. As displayed in Figure 6C, when 100 nM let-7a, miRNA-155, and miRNA-21 were interpolated separately, the signal responses were almost in accordance with that of the blank group, proving the fact that the trigger signal conversion failed. On the contrary, when only 1 nM target miRNA-141 participated in the mixed-solution reaction, the ECL signal of the system decreased significantly, which indicated that the presence of the target could accurately trigger the switch of signal conversion and proved that the biosensor possessed superior sensitivity and accurate selectivity.

https://doi.org/10.1021/acsami.2c08823
ACS Appl. Mater. Interfaces 2022, 14, 32960−32969

Since stability was one of the critical factors to characterize the biosensor, the transformation of the ECL signal of the biosensor was performed in different biological environments. Six groups of biosensor platforms were placed in the environment of 25 and 4 °C, respectively, for 4 weeks, and the numerical fluctuation of the ECL signal was detected every week (Figure 6D). The experimental results certificated that the designed ECL biosensor was provided with good stability both at room temperature and in the refrigerator, which also proved that it could be operated stably for a long time. Moreover, the reproducibility and the analysis in real human serum samples of the biosensor were also discussed (see the Supporting Information).

4. CONCLUSIONS

In summary, the multistrategy cooperative ECL sensing platform on the basis of CRISPR/Cas12a flanking cleavage triumphantly accomplished the detection of miRNA-141. The platform accommodated the improvements of nanoemitter, response implementer, and sensing method that dominated the sensitivity, selectivity, and stability meaningfully. The Co_3O_4@Au NP polyhedron is not only equipped with high conductivity, which provides a suitable active site for biomolecular loading, but also is represented as a signal transmitter to improve the anode emission efficiency of $Ru(bpy)_3^{2+}$ dramatically. Furthermore, the nucleic acid nanoorbital was designed to trigger the HCR to realize the rapid in situ signal accumulation of luminescent $Ru(bpy)_3^{2+}$. Additionally, the CRISPR/Cas12a system with cis and trans cutting properties motivated the implementation of S2-$Ru(bpy)_3^{2+}$ shedding that further avoided the problem of interference factor pollution. Therefore, this method contributed to the construction of a highly sensitive biosensor based on isothermal amplification and fast signal conversion and promised an attractive potential for the combination of CRISPR/Cas12a with clinical molecular diagnostic and biochemical research.

■ ASSOCIATED CONTENT

Supporting Information

The Supporting Information is available free of charge at https://pubs.acs.org/doi/10.1021/acsami.2c08823.

Reagents and instruments; design and fabrication of the LPD; preparation of Au NP seed solution; optimized conditions of the biosensor; reproducibility characterization of the biosensor; real samples analysis; and comparison of different detection methods (PDF)

■ AUTHOR INFORMATION

Corresponding Authors

Li Xie − *Shandong Cancer Hospital and Institute, Shandong First Medical University and Shandong Academy of Medical Sciences, Jinan 250117, P. R. China*; Email: l_xie2001@126.com

Shenguang Ge − *Institute for Advanced Interdisciplinary Research, University of Jinan, Jinan 250022, P. R. China*; orcid.org/0000-0002-0537-6491; Phone: +86-531-82767161; Email: chm_gesg@163.com

Authors

Qian Wang − *Institute for Advanced Interdisciplinary Research, University of Jinan, Jinan 250022, P. R. China; School of Chemistry and Chemical Engineering, University of Jinan, Jinan 250022, P. R. China*

Zuhao Zhang − *Institute for Advanced Interdisciplinary Research, University of Jinan, Jinan 250022, P. R. China*

Lu Zhang − *Institute for Advanced Interdisciplinary Research, University of Jinan, Jinan 250022, P. R. China*

Yunqing Liu − *Institute for Advanced Interdisciplinary Research, University of Jinan, Jinan 250022, P. R. China*

Jinghua Yu − *School of Chemistry and Chemical Engineering, University of Jinan, Jinan 250022, P. R. China*

Complete contact information is available at: https://pubs.acs.org/10.1021/acsami.2c08823

Author Contributions

‖Q.W. and Z.Z. contributed equally to this paper.

Notes

The authors declare no competing financial interest.

■ ACKNOWLEDGMENTS

This work was supported by the National Natural Science Foundation of China (22074053 and 21874055); the Excellent Youth Innovation Team in Universities of Shandong (2019KJC016); the Project of "20 Items of University" of Jinan (2020GXRC047 and 2018GXRC001); the Major Scientific and Technological Innovation Project of Shandong Province (2021CXGC010603); and the Taishan Scholars program and Case-by-Case Project for Top Outstanding Talents of Jinan.

■ REFERENCES

(1) Hu, Q.; Luo, Y.; Cao, X.; Chen, Z.; Huang, Y.; Niu, L. Bioinspired Electro-RAFT Polymerization for Electrochemical Sensing of Nucleic Acids. *ACS Appl. Mater. Interfaces* **2021**, *13*, 54794−54800.

(2) Ranjan, P.; Sadique, M. A.; Yadav, S.; Khan, R. An Electrochemical Immunosensor Based on Gold-Graphene Oxide Nanocomposites with Ionic Liquid for Detecting the Breast Cancer CD44 Biomarker. *ACS Appl. Mater. Interfaces* **2022**, *14*, 20802−20812.

(3) Wang, J. M.; Yao, L. Y.; Huang, W.; Yang, Y.; Liang, W. B.; Yuan, R.; Xiao, D. R. Overcoming Aggregation-Induced Quenching by Metal-Organic Framework for Electrochemiluminescence (ECL) Enhancement: Zn-PTC as a New ECL Emitter for Ultrasensitive MicroRNAs Detection. *ACS Appl. Mater. Interfaces* **2021**, *13*, 44079−44085.

(4) Liu, G.; Hong, J.; Ma, K.; Wan, Y.; Zhang, X.; Huang, Y.; Kang, K.; Yang, M.; Chen, J.; Deng, S. Porphyrin Trio-Pendant Fullerene Guest as an In Situ Universal Probe of High ECL Efficiency for Sensitive miRNA Detection. *Biosens. Bioelectron.* **2020**, *150*, No. 111963.

(5) Zhang, X.; Nie, Y.; Zhang, Q.; Liang, Z.; Wang, P.; Ma, Q. Polydopamine Nanoparticles@MoS_2 Nanosheet Aerogel-based ECL Sensing System for MiRNA-126 Detection. *Chem. Eng. J.* **2021**, *411*, No. 128428.

(6) Simoska, O.; Sans, M.; Fitzpatrick, M. D.; Crittenden, C. M.; Eberlin, L. S.; Shear, J. B.; Stevenson, K. J. Real-Time Electrochemical Detection of Pseudomonas aeruginosa Phenazine Metabolites Using Transparent Carbon Ultramicroelectrode Arrays. *ACS Sens.* **2019**, *4*, 170−179.

(7) Xue, J.; Yang, L.; Jia, Y.; Zhang, Y.; Wu, D.; Ma, H.; Hu, L.; Wei, Q.; Ju, H. Dual-Quenching Electrochemiluminescence Resonance Energy Transfer System from Ru-In_2S_3 to Alpha-MoO_3-Au Based on Protect of Protein Bioactivity for Procalcitonin Detection. *Biosens. Bioelectron.* **2019**, *142*, No. 111524.

(8) Ma, L.; Chen, Y. L.; Song, X. P.; Yang, D. J.; Li, H. X.; Ding, S. J.; Xiong, L.; Qin, P. L.; Chen, X. B. Structure-Adjustable Gold Nanoingots with Strong Plasmon Coupling and Magnetic Resonance for Improved Photocatalytic Activity and SERS. *ACS Appl. Mater. Interfaces* **2020**, *12*, 38554−38562.
(9) Qi, T.; Song, C.; He, J.; Shen, W.; Kong, D.; Shi, H.; Tan, L.; Pan, R.; Tang, S.; Lee, H. K. Highly Sensitive Detection of Multiple MicroRNAs by High-Performance Liquid Chromatography Coupled with Long and Short Probe-Based Recycling Amplification. *Anal. Chem.* **2020**, *92*, 5033−5040.
(10) Li, F.; Xu, M.; Zhuang, J. Dual Biomineralized Metal-organic Frameworks-Mediated Conversion of Chemical Energy to Electricity Enabling Portable PEC Sensing of Telomerase Activity in Bladder Cancer Tissues. *Biosens. Bioelectron.* **2022**, *204*, No. 114070.
(11) Kim, H. R.; Bong, J. H.; Park, J. H.; Song, Z.; Kang, M. J.; Son, D. H.; Pyun, J. C. Cesium Lead Bromide ($CsPbBr_3$) Perovskite Quantum Dot-Based Photosensor for Chemiluminescence Immunoassays. *ACS Appl. Mater. Interfaces* **2021**, *13*, 29392−29405.
(12) Liu, D.; Zhang, X.; Zhao, J.; Chen, S.; Yuan, R. An Ultrasensitive Sensing Platform for MicroRNA-155 Based on H_2O_2 Quenched Hydroxide-dependent ECL Emission of PFO Pdots. *Biosens. Bioelectron.* **2020**, *150*, No. 111872.
(13) Rebeccani, S.; Zanut, A.; Santo, C. I.; Valenti, G.; Paolucci, F. A Guide Inside Electrochemiluminescent Microscopy Mechanisms for Analytical Performance Improvement. *Anal. Chem.* **2022**, *94*, 336−348.
(14) Lee, S.; Cho, W. S.; Park, J. Y.; Lee, H. J.; Lee, J. L.; Lee, K. H.; Hong, K. Water Washable and Flexible Light-Emitting Fibers Based on Electrochemiluminescent Gels. *ACS Appl. Mater. Interfaces* **2022**, *14*, 17709−17718.
(15) Wang, Y.; Darling, S. B.; Chen, J. Selectivity of Per-and Polyfluoroalkyl Substance Sensors and Sorbents in Water. *ACS Appl. Mater. Interfaces* **2021**, *13*, 60789−60814.
(16) Cai, J.; Chen, T.; Xu, Y.; Wei, S.; Huang, W.; Liu, R.; Liu, J. A Versatile Signal-Enhanced ECL Sensing Platform Based on Molecular Imprinting Technique via PET-RAFT Cross-linking Polymerization Using Bifunctional Ruthenium Complex as Both Catalyst and Sensing Probes. *Biosens. Bioelectron.* **2019**, *124*−*125*, 15−24.
(17) Guo, X.; Lie, Q.; Liu, Y.; Jia, Z.; Gong, Y.; Yuan, X.; Liu, J. Multifunctional Selenium Quantum Dots for the Treatment of Alzheimer's Disease by Reducing Abeta-Neurotoxicity and Oxidative Stress and Alleviate Neuroinflammation. *ACS Appl. Mater. Interfaces* **2021**, *13*, 30261−30273.
(18) Li, X.; Wu, D.; Ma, H.; Wang, H.; Wang, Y.; Fan, D.; Du, B.; Wei, Q.; Zhang, N. Ultrasensitive Amyloid-beta Proteins Detection Based on Curcumin Conjugated ZnO Nanoparticles Quenching Electrochemiluminescence Behavior of Luminol Immobilized on $Au@MoS_2/Bi_2S_3$ Nanorods. *Biosens. Bioelectron.* **2019**, *131*, 136−142.
(19) Chen, J. X.; Zhuo, Y.; Peng, X.; Chai, Y. Q.; Yuan, R.; Liang, W. B. A Dynamic DNA Machine via Free Walker Movement on Lipid Bilayer for Ultrasensitive Electrochemiluminescent Bioassay. *Anal. Chem.* **2019**, *91*, 14125−14132.
(20) Yao, B.; Zhang, J.; Fan, Z.; Ding, Y.; Zhou, B.; Yang, R.; Zhao, J.; Zhang, K. Rational Engineering of the DNA Walker Amplification Strategy by Using a $Au@Ti_3C_2@PEI\text{-}Ru(dcbpy)_3^{(2+)}$ Nanocomposite Biosensor for Detection of the SARS-CoV-2 RdRp Gene. *ACS Appl. Mater. Interfaces* **2021**, *13*, 19816−19824.
(21) Ning, Z.; Zheng, Y.; Pan, D.; Zhang, Y.; Shen, Y. Coupling Aptazyme and Catalytic Hairpin Assembly for Cascaded Dual Signal Amplified Electrochemiluminescence Biosensing. *Biosens. Bioelectron.* **2020**, *150*, No. 111945.
(22) Ma, J.; Wu, L.; Li, Z.; Lu, Z.; Yin, W.; Nie, A.; Ding, F.; Wang, B.; Han, H. Versatile Electrochemiluminescence Assays for PEDV Antibody Based on Rolling Circle Amplification and Ru-DNA Nanotags. *Anal. Chem.* **2018**, *90*, 7415−7421.
(23) Wu, D.; Xin, X.; Pang, X.; Pietraszkiewicz, M.; Hozyst, R.; Sun, X.; Wei, Q. Application of Europium Multiwalled Carbon Nanotubes as Novel Luminophores in an Electrochemiluminescent Aptasensor for Thrombin Using Multiple Amplification Strategies. *ACS Appl. Mater. Interfaces* **2015**, *7*, 12663−12670.
(24) Li, Y.; Wang, L.; Ding, C.; Luo, X. Highly Selective Ratiometric Electrogenerated Chemiluminescence Assay of DNA Methyltransferase Activity via Polyaniline and Anti-fouling Peptide Modified Electrode. *Biosens. Bioelectron.* **2019**, *142*, No. 111553.
(25) Mi, X.; Li, H.; Tan, R.; Feng, B.; Tu, Y. The TDs/aptamer cTnI Biosensors Based on HCR and Au/Ti_3C_2-MXene Amplification for Screening Serious Patient in COVID-19 Pandemic. *Biosens. Bioelectron.* **2021**, *192*, No. 113482.
(26) Peng, X.; Zhu, J.; Wen, W.; Bao, T.; Zhang, X.; He, H.; Wang, S. Silver Nanoclusters-assisted Triple-amplified Biosensor for Ultrasensitive Methyltransferase Activity Detection Based on AuNPs/ERGO Hybrids and Hybridization Chain Reaction. *Biosens. Bioelectron.* **2018**, *118*, 174−180.
(27) Liu, F. X.; Cui, J. Q.; Park, H.; Chan, K. W.; Leung, T.; Tang, B. Z.; Yao, S. Isothermal Background-Free Nucleic Acid Quantification by a One-Pot Cas13a Assay Using Droplet Microfluidics. *Anal. Chem.* **2022**, *94*, 5883−5892.
(28) Luo, T.; Li, J.; He, Y.; Liu, H.; Deng, Z.; Long, X.; Wan, Q.; Ding, J.; Gong, Z.; Yang, Y.; Zhong, S. Designing a CRISPR/Cas12a- and Au-Nanobeacon-Based Diagnostic Biosensor Enabling Direct, Rapid, and Sensitive miRNA Detection. *Anal. Chem.* **2022**, *94*, 6566−6573.
(29) Deng, H. X.; Zhai, H.; Shi, Y.; Liu, G.; Lowry, J.; Liu, B.; Ryan, E. B.; Yan, J.; Yang, Y.; Zhang, N.; Yang, Z.; Liu, E.; Ma, Y. C.; Siddique, T. Efficacy and Long-term Safety of CRISPR/Cas9 Genome Editing in the SOD1-linked Mouse Models of ALS. *Commun. Biol.* **2021**, *4*, 396.
(30) Broughton, J. P.; Deng, X.; Yu, G.; Fasching, C. L.; Servellita, V.; Singh, J.; Miao, X.; Streithorst, J. A.; Granados, A.; Sotomayor-Gonzalez, A.; Zorn, K.; Gopez, A.; Hsu, E.; Gu, W.; Miller, S.; Pan, C. Y.; Guevara, H.; Wadford, D. A.; Chen, J. S.; Chiu, C. Y. CRISPR-Cas12-based Detection of SARS-CoV-2. *Nat. Biotechnol.* **2020**, *38*, 870−874.
(31) Zhang, Y.; Wu, Y.; Wu, Y.; Chang, Y.; Liu, M. CRISPR-Cas systems: From Gene Scissors to Programmable Biosensors. *TrAC, Trends Anal. Chem.* **2021**, *137*, No. 116210.
(32) Qin, P.; Park, M.; Alfson, K. J.; Tamhankar, M.; Carrion, R.; Patterson, J. L.; Griffiths, A.; He, Q.; Yildiz, A.; Mathies, R.; Du, K. Rapid and Fully Microfluidic Ebola Virus Detection with CRISPR-Cas13a. *ACS Sens.* **2019**, *4*, 1048−1054.
(33) Han, C.; Li, W.; Li, Q.; Xing, W.; Luo, H.; Ji, H.; Fang, X.; Luo, Z.; Zhang, L. CRISPR/Cas12a-Derived Electrochemical Aptasensor for Ultrasensitive Detection of COVID-19 Nucleocapsid Protein. *Biosens. Bioelectron.* **2022**, *200*, No. 113922.
(34) Li, H.; Li, M.; Yang, Y.; Wang, F.; Wang, F.; Li, C. Aptamer-Linked CRISPR/Cas12a-Based Immunoassay. *Anal. Chem.* **2021**, *93*, 3209−3216.
(35) Liu, C.; Ren, L.; Li, X.; Fan, N.; Chen, J.; Zhang, D.; Yang, W.; Ding, S.; Xu, W.; Min, X. Self-electrochemiluminescence Biosensor Based on CRISPR/Cas12a and PdCuBP@luminol Nanoemitter for Highly Sensitive Detection of Cytochrome C Oxidase Subunit III Gene of Acute Kidney Injury. *Biosens. Bioelectron.* **2022**, *207*, No. 114207.
(36) Chen, K.; Li, W.; Zhu, C.; Yuan, L. Construction of Hollow Cobalt Tetroxide Nanocages through the Metal Salt Bifunctional Etching Strategy for Catalytic Oxidation of Propane at Ultrahigh Space Velocity. *ACS Appl. Nano Mater.* **2022**, *5*, 6575−6584.
(37) Cui, K.; Zhou, C.; Zhang, B.; Zhang, L.; Liu, Y.; Hao, S.; Tang, X.; Huang, Y.; Yu, J. Enhanced Catalytic Activity Induced by the Nanostructuring Effect in Pd Decoration onto Doped Ceria Enabling an Origami Paper Analytical Device for High Performance of Amyloid-beta Bioassay. *ACS Appl. Mater. Interfaces* **2021**, *13*, 33937−33947.
(38) Ming, T.; Luo, J.; Liu, J.; Sun, S.; Xing, Y.; Wang, H.; Xiao, G.; Deng, Y.; Cheng, Y.; Yang, Z.; Jin, H.; Cai, X. Paper-based Microfluidic Aptasensors. *Biosens. Bioelectron.* **2020**, *170*, No. 112649.

(39) Zheng, X.; Li, L.; Cui, K.; Zhang, Y.; Zhang, L.; Ge, S.; Yu, J. Ultrasensitive Enzyme-free Biosensor by Coupling Cyclodextrin Functionalized Au Nanoparticles and High-Performance Au-Paper Electrode. *ACS Appl. Mater. Interfaces* **2018**, *10*, 3333−3340.
(40) Li, X.; Li, Y.; Zhang, J.; Meng, Y.; Yu, X.; Wang, X.; Hun, X. Molybdenum Disulfide/graphdiyne-based Photoactive Material Derived Photoelectrochemical Strategy for Highly Sensitive MicroRNA Assay. *Sens. Actuators, B* **2019**, *297*, No. 126808.
(41) Nie, D.; Zhang, Z.; Guo, D.; Tang, Y.; Hu, X.; Huang, Q.; Zhao, Z.; Han, Z. A Flexible Assay Strategy for Non-glucose Targets Based on Sulfhydryl-terminated Liposomes Combined with Personal Glucometer. *Biosens. Bioelectron.* **2021**, *175*, No. 112884.
(42) Tian, J. K.; Zhao, M. L.; Song, Y. M.; Zhong, X.; Yuan, R.; Zhuo, Y. MicroRNA-Triggered Deconstruction of Field-Free Spherical Nucleic Acid as an Electrochemiluminescence Biosensing Switch. *Anal. Chem.* **2021**, *93*, 13928−13934.
(43) Xiong, C.; Zhang, T.; Kong, W.; Zhang, Z.; Qu, H.; Chen, W.; Wang, Y.; Luo, L.; Zheng, L. ZIF-67 Derived Porous Co_3O_4 Hollow Nanopolyhedron Functionalized Solution-gated Graphene Transistors for Simultaneous Detection of Glucose and Uric Acid in Tears. *Biosens. Bioelectron.* **2018**, *101*, 21−28.
(44) Fytianos, K.; Chortarea, S.; Rodriguez-Lorenzo, L.; Blank, F.; von Garnier, C.; Petri-Fink, A.; Rothen-Rutishauser, B. Aerosol Delivery of Functionalized Gold Nanoparticles Target and Activate Dendritic Cells in a 3D Lung Cellular Model. *ACS Nano* **2017**, *11*, 375−383.

https://doi.org/10.1021/acsami.2c08823
ACS Appl. Mater. Interfaces 2022, 14, 32960−32969